# Supplementary Information for ”Interrogating helical nanorod self-assembly with fractionated cellulose nanocrystal suspensions”

Camila Honorato-Rios and Jan P.F. Lagerwall

July 29, 2020

## Supplementary Note 1:
## General characterization of the as-received CNCs

This section describes the characterization of the CNC batch used for the 20/80 fractionation. The batch used for the 50/50 fractionation was the same as used in our previous fractionation study [1], hence we refer the reader to that paper for its characterization.

### Conductivity and pH

The conductivity and pH of the pristine CNC suspension at 20°C are plotted as a function of CNC mass concentration in Fig. 1.

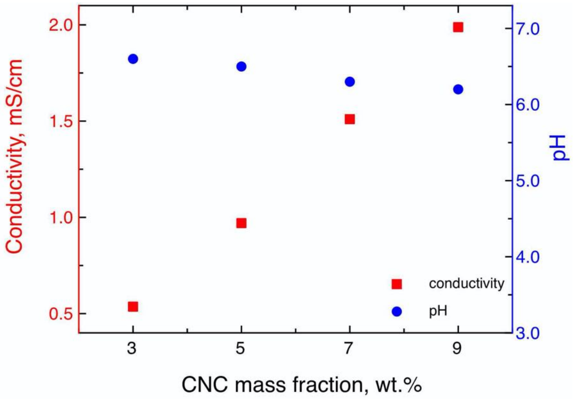

Supplementary Figure 1: Values of conductivity and pH for the as-received CNC at different mass concentrations.

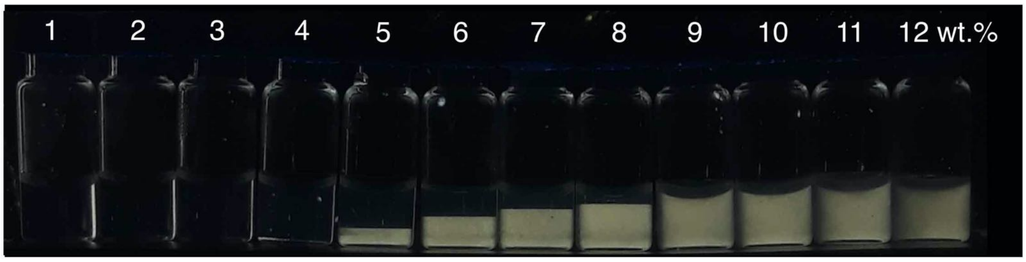

Supplementary Figure 2: Macroscopic phase separation in a series of CNC suspensions with increasing global CNC mass concentrations $W$, after protonation by ion-exchange process. The sample vials were photographed three weeks after preparation.

## Determination of the concentration of sulphate half-ester groups by conductometric titration

For the determination of the negative surface charges of the CNCs (sulphate half-ester groups), we followed the procedure reported by Beck, *et al* [2], which consists of a purification step (dialysis), protonation via an ion-exchange column and conductometric titration for the final determination of the charges. Since every sulphate half ester releases one $Na^+$ counter ion into solution, this study also provides information about the counter ion content of the aqueous phase as a function of CNC content.

### Dialysis and sonication

The as-received CNC suspension is first dialysed in ultra pure water (water conductivity of 0.05 S/cm) during 5 days at a CNC mass concentration of $W = 2$ wt.%. After this time, the dialysed suspension is subjected to sonication as described in the Methods section in the main manuscript. The final pH is 4.2.

### Ion-exchange column

The critical factor for an accurate determination of the negative surface charges in CNC suspensions is the complete protonation of the sample. To achieve this, a glass column (inner diameter 2.5 cm) with fritted glass disk at the bottom was partially filled with 40 g of $H^+$ form resin (DOWEX 50WX8, Sigma Aldrich) previously slurried with ultra pure water. The column was fed with the dialysed and sonicated CNC suspension diluted to 0.5 wt.%, yielding a pH after the ion-exchange process of 2.7. Phase separation in this protonated CNC suspension series is shown in Fig. 2.

### Conductometric titration

For the final determination of the negative surface charges, 2 mL of 0.1 M NaCl solution is added to 200 mL protonated CNC suspension at 0.1 wt.%. The sample is titrated

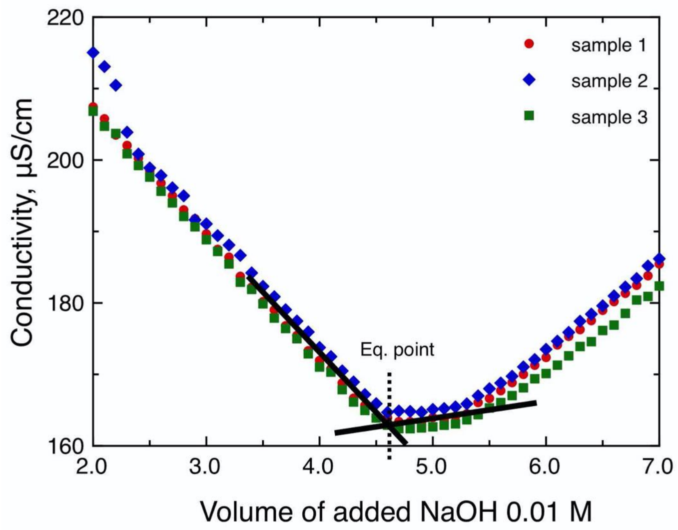

Supplementary Figure 3: Conductometric titration curves for determination of the negative surface charges. The equivalence point (”Eq. point”) obtained from the titration curve gives the sulphur content.

Supplementary Table 1: Equivalence point and calculated sulphur mass concentration for three protonated CNC suspensions.

| Sample | $\mathrm{m}_{CNC}, mg$ | Equivalence point $\mathrm{E}_p, mL$ | $\mathrm{m}_S/m_{CNC}$ |
|---|---|---|---|
| CNC 1 | 150 | 4.6 | 0.010 |
| CNC 2 | 150 | 4.7 | 0.010 |
| CNC 3 | 150 | 4.6 | 0.010 |

with 10 mM NaOH using a T90 Mettler Toledo titrator system in 0.1 mL increments over a period of 20 min.

Figure 3 presents the titration curves for three protonated CNC suspensions. The equivalence point, $E_p$ (”Eq. point” in Figure 3), represents the complete neutralization of the sulphate groups by the base. For the calculation, $c_{NaOH} = 0.01$ M and the molar mass of sulphur $M_S = 32$ g/mol.

The sulphur content of CNC suspensions is determined according to the expression:

$$\frac{m_S}{m_{CNC}} = \frac{E_p c_{NaOH} M_S}{m_{CNC}} \tag{1}$$

where $m_S$ is the mass of sulphur and $m_{CNC}$ the mass of CNC. Based on the results presented in Table 1, the sulphur content in the initial CNC is found to be 1.0 wt.%.

# Supplementary Note 2: Analysis of the geometrical features of CNCs from atomic force microscopy (AFM) data

Before going into the details of the analysis of our CNCs by AFM, we pause briefly to discuss how we can conveniently and appropriately describe the geometry of a CNC. The most detailed investigations of the geometry of dry CNCs that we are aware of are those of Usov et al. [3] (AFM and electron microscopy) and of Majoinen et al. [4] (electron tomography). The latter clearly shows that the cross section is highly irregular, with significant variations in thickness and width, which are generally unequal. Both papers show that, additionally, the overall structure twists along the length of the CNC. These two aspects mean that any individual local measurement of CNC lateral dimension is unlikely to be representative of the lateral dimension of the particle as a whole. It is more appropriate to use an average lateral dimension value, which we may use as diameter in an approximation of the effective CNC shape as a cylindrical rod, being well aware that the actual CNC is more like a twisted irregular ribbon.

The cylindrical approximation becomes particularly appropriate when considering the significance of geometry for macroscopic phase aspects such as phase diagram and helix pitch, as we do in this study. This is because in a colloidal suspension the particles are not standing still, but thermal motion induces considerable translational and rotational motion. In a phase with nematic long-range orientational order, rotation about the main symmetry axis of the particles (the long axis of CNCs) is particularly easy, as it suffers from minimum sterical hindrance, hence we may expect rapid rotations of this kind. While we are not aware of any studies of the long axis rotation frequency in CNC suspensions, the corresponding frequency in thermotropic liquid crystals is in the GHz range. The two orders of magnitude greater length of CNCs will lead to lower rotation frequency, but it will still be fast enough that local variations in lateral dimensions of a CNC are averaged out, and a cylindrical rod approximation is thus appropriate for the discussion in this paper.

It is less obvious how to practically establish the correct average diameter $d$. We are here limited to use the average lateral dimension obtained by AFM, which may underestimate $d$, since the CNCs may tend to adsorb mainly with their width along the substrate. This would mean that $d_{AFM}$ is closer to the thickness than the width of the CNC, although the irregularity in shape and the overall twist make any interpretation of this kind a delicate venture.

## Extraction of representative lengths and lateral dimensions for individual CNCs

In order to obtain representative values of length $L$ and apparent lateral dimension $d_{AFM}$ for the dry CNCs, we measure the height profile along each of 200 individual CNCs from each fraction with the software WSxM, analyzing the data as reported in our previous work [1]. The CNCs have been deposited on a substrate as described in the Methods section of the main paper, hence they are lying with their average long axis paralell to the substrate. To obtain the length $L$ we use the extension in the $x$ and $y$ directions for each CNC ($\Delta x$ and $\Delta y$), which are extracted from the AFM height data, applying the Pythagorean theorem as $L = \sqrt{\Delta x^2 + \Delta y^2}$. In the AFM image presented in Figure 4, with an inset showing the irregular height profile of one CNC, we demonstrate the procedure.

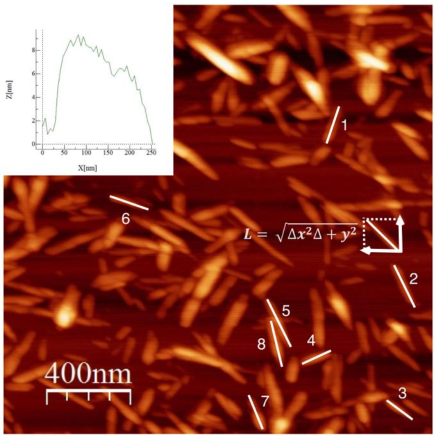

Supplementary Figure 4: Example of the determination of length $L$ and apparent lateral dimension $d_{AFM}$ of dry CNCs by AFM analysis. The inset presents the height profile of one randomly selected CNC, showing the significant variations of $d_{AFM}$ along one and the same CNC.

The significant variation of $d_{AFM}$ along each CNC, reflecting the twisted irregular ribbon character [3, 4], makes it difficult to identify a representative value for the lateral dimension. Therefore, we use the average height along the full length of a CNC to represent its apparent lateral dimension in the dry state. We believe that our procedure is more representative than measuring a single lateral dimension value at one line crossing the CNC, as is otherwise often done.

## Statistical analysis of apparent lateral dimensions, lengths and aspect ratios

The 200 individual $d_{AFM}$ values are averaged, assuming a normal distribution, to obtain a $\bar{d}_{AFM}$-value for each fraction that is as representative as possible. Due to the large variation within each CNC, the resulting average value has a large standard deviation $\sigma$. The final average values of $\bar{d}_{AFM}$ and $\bar{L}$ for each of the fractions are included in Table 1 in the main paper.

For the CNC length we assume a log-normal distribution, as a regular normal distribution tends to have significant tails into unphysical negative length values. This means that we take the logarithm of the length and consider this to follow a normal distribution. The probability distribution function for the log-normal distribution can be written:

$$P(L) = \frac{1}{L\varsigma\sqrt{2\pi}} e^{-(\ln L - \mu)^2/(2\varsigma^2)} \qquad (2)$$

where $\varsigma$ and $\mu$ are the standard deviation and mean value of $\ln L$. What interests us more is the average CNC length, which is obtained as $\bar{L} = e^{(\mu+\varsigma^2/2)}$, and the length dispersity, which is generally defined as the standard deviation of $L$ divided by $\bar{L}$. Since we are not using a normal distribution, we need to consider the variance $\sigma^2$ of $L$ which for the log-normal distribution can be written $\sigma^2 = [e^{\varsigma^2-1}]e^{2(\mu+\varsigma^2/2)}$. We can thus write the dispersity as:

$$\text{Dispersity} = \frac{\sqrt{\sigma^2}}{\bar{L}} = \frac{\sqrt{[e^{\varsigma^2-1}]e^{2(\mu+\varsigma^2/2)}}}{e^{(\mu+\varsigma^2/2)}} = \sqrt{e^{\varsigma^2-1}} \approx \sqrt{1+\varsigma^2-1} = \varsigma \qquad (3)$$

where we in the last step expanded the exponential with only one term, motivated by the fact that $\varsigma$ is small, with its square even smaller. In other words, the parameter $\varsigma$ of the log-normal distribution has the convenient property of providing us with the dispersity of the CNC length distribution. The experimentally obtained length distributions for all fractions, obtained as described above, are summarized together with the results of fitting the log-normal distribution to the experimental data as well as the raw AFM images in Fig. 5.

Because of the very large uncertainty in $\bar{d}_{AFM}$, and its enormous impact on the CNC aspect ratio arising from its low value and its position in the denominator, it is actually more misleading than helpful to provide values for the CNC aspect ratio. We give the range of aspect ratios for each fraction, corresponding to the maximum and minimum value of $\bar{d}_{AFM}$, in Table 1, but in the paper we focus on the CNC lengths, where we can clearly see a systematic change as a result of fractionation. Based on the experimental data, we consider the apparent CNC lateral dimension to be approximately unaffected by fractionation. The key reasons for this are, we believe, the significant variations in lateral extension *within* each CNC, and the fact that CNCs are far from perfect cylindrical rods. This means that a well-defined lateral dimension does not really exist, but we can probably consider a value of 4–5 nm as representative for all CNCs within an approximative treatment of the CNCs as cylindrical rods. Nevertheless, we point out that there may be variations in the effective lateral dimension between fractions that are too small for us to detect.

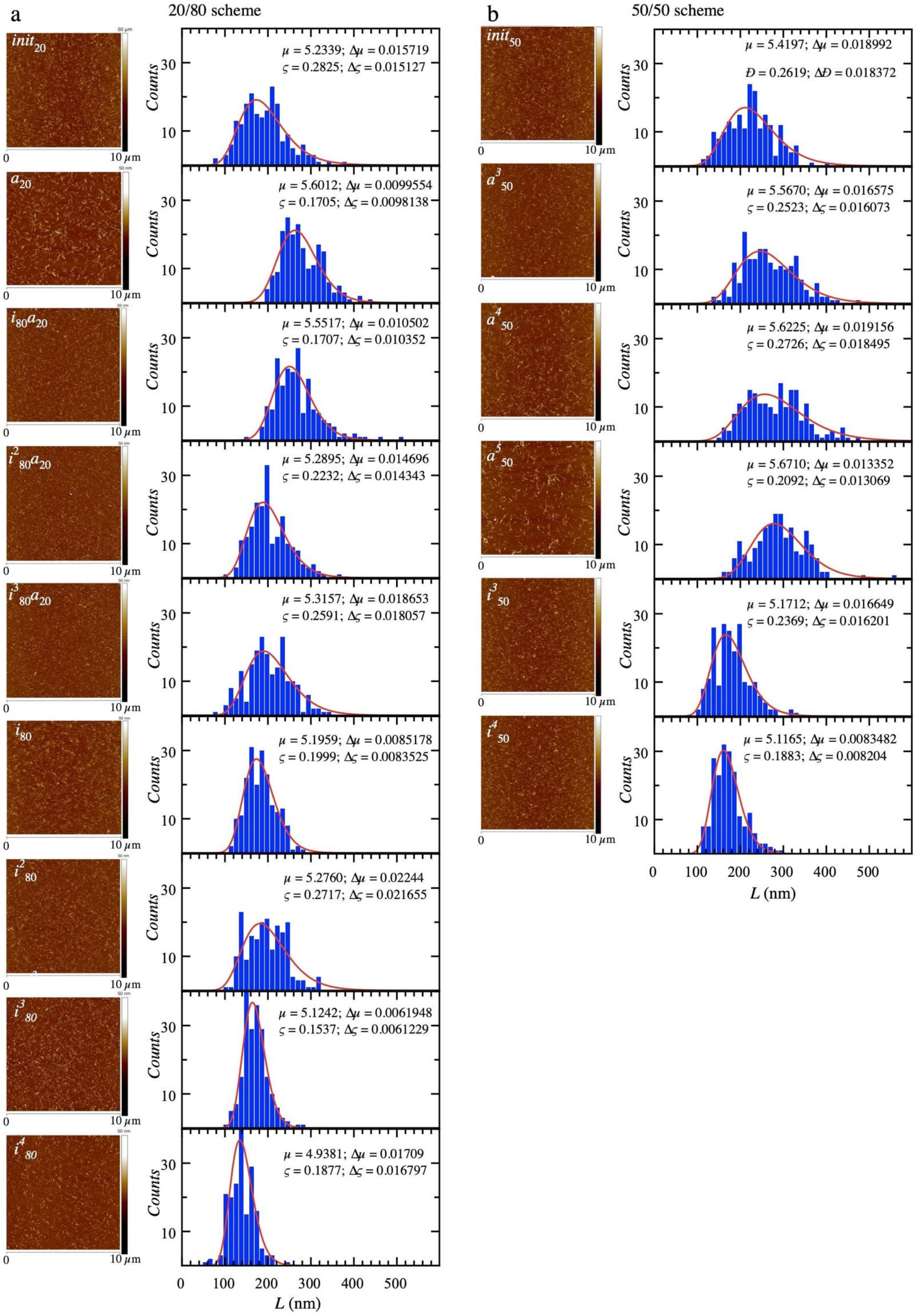

Supplementary Figure 5: AFM images of CNCs from the initial suspensions and from all fractions, together with a log-normal distribution statistical analysis of rod lengths. The numerical fitting results are indicated in each diagram.

# Supplementary Note 3: Establishment of the target mass concentrations for each step of fractionation

## The 20/80 scheme

For establishing $W$ for which the anisotropic volume fraction $\Phi \approx 20$ vol.%, we prepared series of overall mass concentrations in the range between 1 wt.% and 11 wt.%. Each CNC sample was prepared by concentrating, under mild mechanical stirring, a small volume of the respective isotropic phase that remained in the separatory funnel after the anisotropic part had been drained out.

Specifically, as we explained in Methods, an initial CNC suspension ($init_{20}$) at $W =$ 5.5 wt.% was filled into a separatory funnel, which corresponds to $\Phi \approx 20$ vol.%, as shown in Fig. 1d–e in the main paper. After the separation of the phases, 15 g of the upper phase $i_{80}$ was concentrated to $W = 11$ wt.% followed by the preparation of a sample series between 1 wt.% and 11 wt.%. After 5 days, we identified that $W = 6$ wt.% yields an anisotropic volume fraction of $\Phi \approx 20$ vol/% in $i_{80}$. With this information, the separatory funnel was filled with the remaining $i_{80}$ sample after concentrating it to $W = 6$ wt.% (Fig. 1c in the main manuscript). This was then phase separated into $i_{80}a_{20}$ and $i^2_{80}$. We performed the same procedure for the remaining isotropic phases ($i^2_{80}$ and $i^3_{80}$), finding the target mass concentrations $W = 7$ wt.% and $W = 8$ wt.%, respectively. Phase separation in the separatory funnel with these suspensions resulted in the fractions $i^2_{80}a_{20}$ and $i^3_{80}a_{20}$, respectively.

## The 50/50 scheme

For the preparation of the $a^n_{50}$ fractions (Fig. 1b in the main manuscript), an initial CNC suspension ($init_{50}$) with an anisotropic volume fraction of 50 vol.% at $W = 6$ wt.% was filled into a separatory funnel. The lower part ($a^1_{50}$) was drained out and 15 g was concentrated by mechanical stirring to $W=$ 11 wt.% under room conditions. Afterwards, a sample series was prepared in a mass concentration range between 1 wt.% and 11 wt.% by the addition of ultra pure water. After 5 days we identified that $W=$ 5.5 wt.% yields $\Phi \approx 50$ vol.% for the $a^1_{50}$ fraction. Having this information, the remaining $a^1_{50}$ sample was diluted to $W=$ 5.5 wt.% and filled into a new separatory funnel, which resulted in $a^2_{50}$. The same procedure with the $\Phi \approx 50$ vol.% target was carried out for the preparation of $a^3_{50}$, $a^4_{50}$ and $a^5_{50}$ fractions, resulting in $W = 5$ wt.% ($a^2_{50} \rightarrow a^3_{50}$), $W=$ 3.8 wt.% ($a^3_{50} \rightarrow a^4_{50}$) and $W=$ 3.6 wt.% ($a^4_{50} \rightarrow a^5_{50}$), respectively. The isotropic fractions from each separation beyond the first step were rejected.

For the preparation of the $i^n_{50}$ fractions, 15 g of the upper part of $init_{50}$ that remained in the separatory funnel ($i^1_{50}$) after the extraction of $a^1_{50}$ was concentrated to $W=$ 11 wt.%. The sample was stirred in a beaker under room conditions. A sample series was prepared by the addition of ultra pure water in a mass concentration range between 1 wt.% and 11 wt.%. After 5 days we identified that $W=$ 7 wt.% yields $\Phi \approx 50$ vol.% for the $i^1_{50}$ fraction. The remaining $i^1_{50}$ sample was then concentrated to $W=$ 7 wt.% and filled into a new separatory funnel, which resulted in an upper phase referred to as $i^2_{50}$. The same procedure with the $\Phi \approx 50$ vol.% target was followed for the preparation of the $i^3_{50}$ and $i^4_{50}$ fractions, resulting in $W=$ 8 wt.% ($i^2_{50} \to i^3_{50}$) and $W=$ 9 wt.% ($i^3_{50} \to i^4_{50}$), respectively. The anisotropic fractions from each separation beyond the first step were rejected.

## Supplementary Note 4: Experimental analysis of the biphasic regime of each fraction

For each initial CNC suspension and for each fraction derived according to the two fractionation schemes, we prepare vials with $W$ varying from 1–11 or 1–12 wt.%, see Fig. 6-7. The vials have been standing undisturbed vertically for 1 month before taking the photos with black background in this figure. These photos are obtained with the vials between crossed polarisers of high quality. The photos with blue background are taken with the vials between crossed polarisers of medium quality, not giving complete extinction. This is actually an advantage, as it makes it easier to estimate the volume fraction of anisotropic phase. Moreover, the photos with blue background were taken significantly later, 10 months after preparation. Unfortunately the samples obtained via the 50/50 scheme were not saved after the initial investigation, hence all photos of these series are with black background. Among the samples obtained via the 20/80 scheme, four series were disturbed from their vertical orientation during long-term storage, hence we use the 1-month photographs with black background also for these series.

To estimate the volume fraction of cholesteric phase in each biphasic sample, a rectangle is drawn that approximates the average total sample height $h_t$ (black lines on blue background or white on black background) and another rectangle (red) is drawn to estimate the height $h_a$ of the anisotropic phase fraction. The heights in length units of the graphics software are indicated next to each rectangle, in the same colour. The volume fraction of anisotropic phase is then obtained as:

$$\Phi = h_a/h_t,$$

since the vial cross section area is constant.

For low $W$, where the phase separation is completed, the error is attributed to the accuracy in the technique used for estimating the volume fraction, as just described. The rectangles for anisotropic and total volumes are each changed by one step in the graphics software, in opposite directions, and the mismatch from the measured value for the volume fraction is used as the error. For large $W$, it is clear that phase separation is not completed, and it will not complete even if waiting very long time. The error is therefore estimated by judging by eye how much anisotropic tactoids remain in the isotropic phase, the fraction of which constitutes the dominant error. Note that the error can be considered symmetric, as isotropic atactoids in the lower phase cannot be visualized, although they contribute to the error as well.

# 20/80

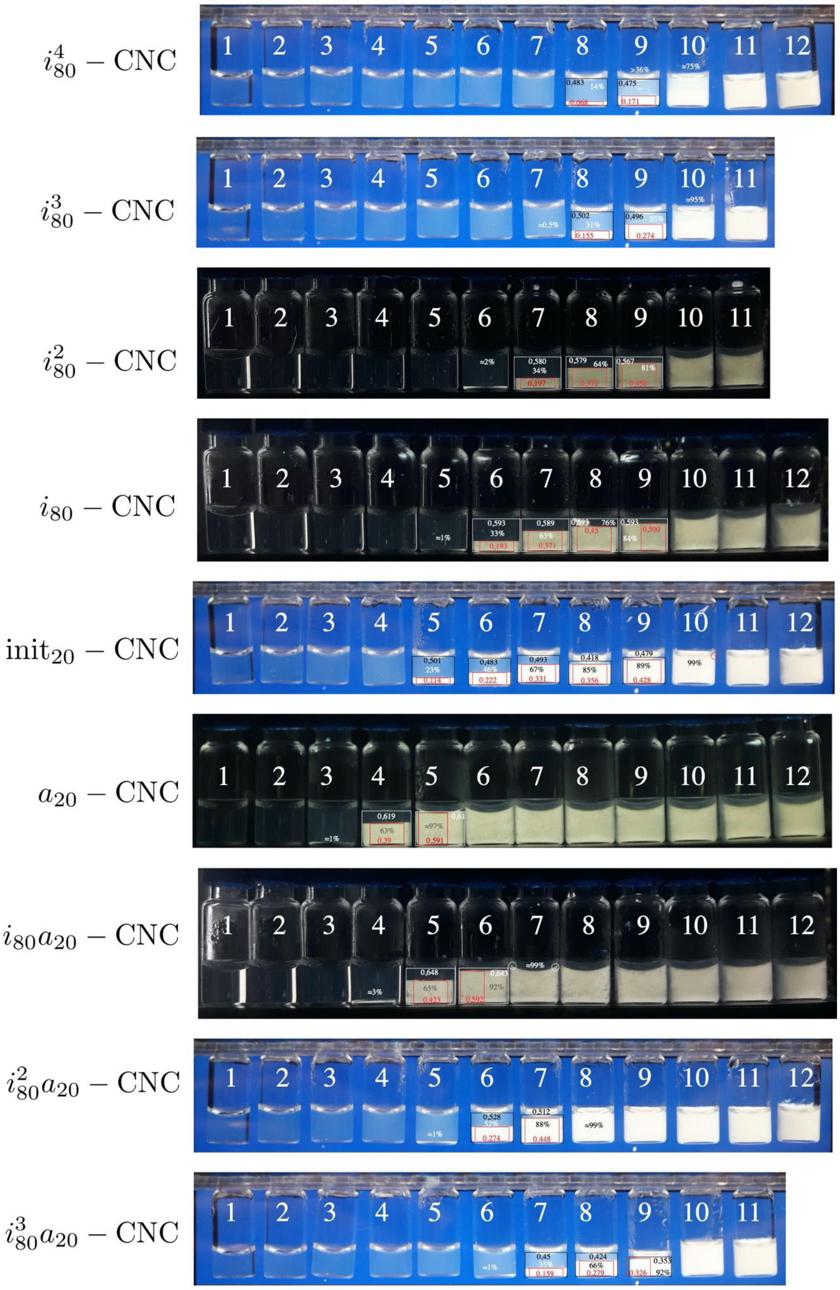

Supplementary Figure 6: CNC suspensions with varying concentrations from each fraction in the 20/80 scheme, for establishing phase separation diagrams. Each vial has a diameter of 11 mm.

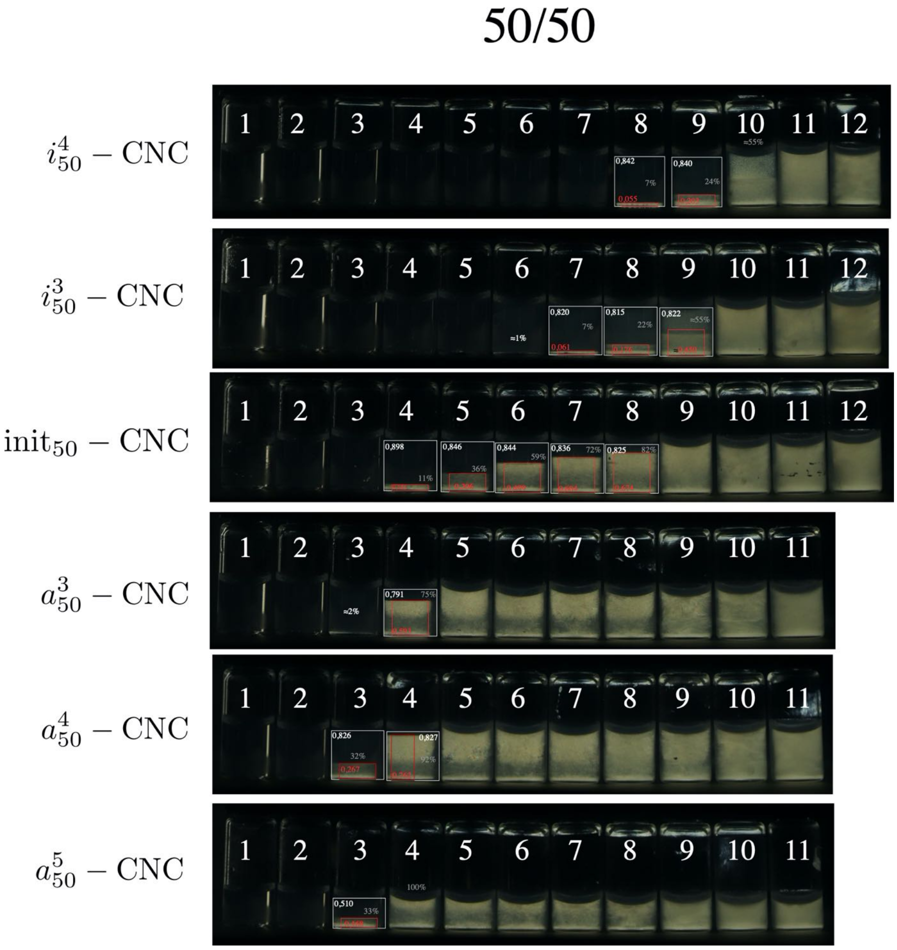

Supplementary Figure 7: CNC suspensions with varying concentrations from each fraction in the 50/50 scheme, for establishing phase separation diagrams. Each vial has a diameter of 11 mm.

## Supplementary Note 5: Phase separation dynamics

### Captions for Supplementary Videos 1 and 2

Video 1 shows a time lapse photography sequence of six vials filled with the $a^3_{50}$-CNC at global sample mass concentrations $W = 2, 3.2, 3.4, 3.6, 3.8$ and 5 wt.%, respectively. The first is fully isotropic, the second to fifth are in the biphasic regime, and the sixth is fully liquid crystalline. The real time between two frames in the video is 2 minutes, thus the full video represents 15 hours in reality. Prior to start, all vials were vortexed vigorously to randomly distribute isotropic and anisotropic domains.

Video 2 shows the corresponding time lapse photography sequence of six vials filled with the $i^3_{50}$-CNC at global sample mass concentrations $W = 6, 7, 8, 9, 10$ and 11 wt.%, respectively, roughly corresponding to the vials in video 1 with respect to their locations in the phase separation diagram. All vials are in the biphasic regime, but the first just barely so, with a very small fraction of anisotropic phase. The last appears as if it were fully liquid crystalline but this is probably not quite true; at this value of $W$ it is very difficult to judge correctly the volume fraction of anisotropic phase, due to the slow dynamics of the short-rod suspensions, as discussed in the main paper. The real time between two frames in the video is 10 minutes, thus the full video represents 12 days in reality. Prior to start, all vials were vortexed vigorously to randomly distribute isotropic and anisotropic domains.

## Long-term study of phase separation in capillaries

To investigate the dynamics of cholesteric liquid crystal self-assembly over long time and on a microscopic scale as a function of CNC length, we fill a long-, intermediate- and short-CNC suspension from each fractionation scheme into 5 cm long glass capillaries with a rectangular cross section of 0.20 mm x 4 mm. The two lowest CNC mass concentrations are chosen in the biphasic regime and the highest concentration is in or near the fully cholesteric range. We carefully glue the capillaries closed, and store them vertically for several months. The capillaries are then investigated by polarising optical microscopy (POM) after 2 months for the 20/80 fractions (Fig. 8) and after 18 months for the 50/50 fractions (Fig. 9).

We focus mainly on the phase separation within the biphasic regime, where the upper isotropic phase is expected to be black and the lower cholesteric (anisotropic) phase would exhibit a characteristic fingerprint and/or 'oily streak' texture (see below). However, such separation is only observed for the samples that contain long rods ($a_{20}$, lowest row in Fig. 8, and $a_{50}^{3}$, lowest row in Fig. 9), a sharp horizontal division between the phases being clearly detectable. For $W > w_1$ (7 wt.% $a_{20}$ in the lower right photo in Fig. 8) the cholesteric texture decorates the entire capillary, as expected for fully liquid crystalline samples.

The sharp phase separation in the biphasic regime is disturbed when working with the shorter rods (two top rows in Fig. 8 and the upper row in Fig. 9). In this case tactoids are present even after 18 months (Fig. 9), especially when the CNC content in the isotropic phase approaches the threshold for kinetic arrest ($w_k \approx 12$ wt.%). The difference in density between cholesteric tactoids and the isotropic phase is then insufficient to drive the separation into two macroscopic separate phases, regardless of the preparation procedure, due to the diverging viscosity of the isotropic phase.

## Near-equilibrium cholesteric texture in long-rod CNC fractions

In the capillaries with long-CNC fractions we note that much, and sometimes all, of the cholesteric texture is uniformly dark, see the lowest rows in Fig. 8 and Fig. 9. This is in contrast to textures commonly seen when unfractionated CNC suspensions are studied by POM in capillaries. The dark texture can be explained by the very low viscosity of the long-CNC cholesteric phase, allowing it to dynamically realign the helix, adopting to

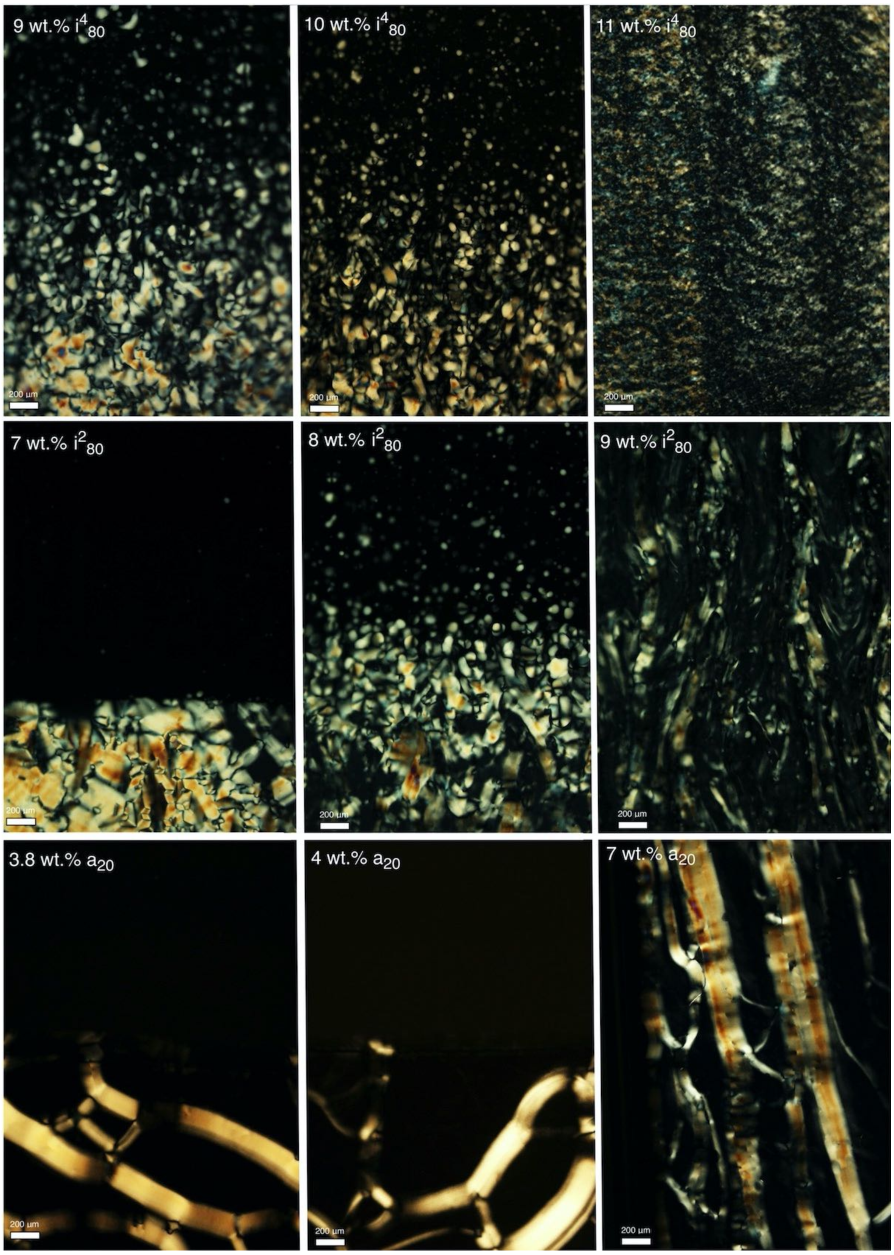

Supplementary Figure 8: Polarising optical microscopy images of vertically stored (2 months) glass capillaries filled with $i^4_{80}$ (top), $i^2_{80}$ (middle) and $a_{20}$ (bottom) fractions from the 20/80 scheme. The CNC content is chosen to be in the middle of the biphasic regime (left), near its boundary to cholesteric (centre) and in or very near the fully cholesteric phase (right). The scale bars correspond to 200 $\mu$m. Gravity is downwards in all photos.

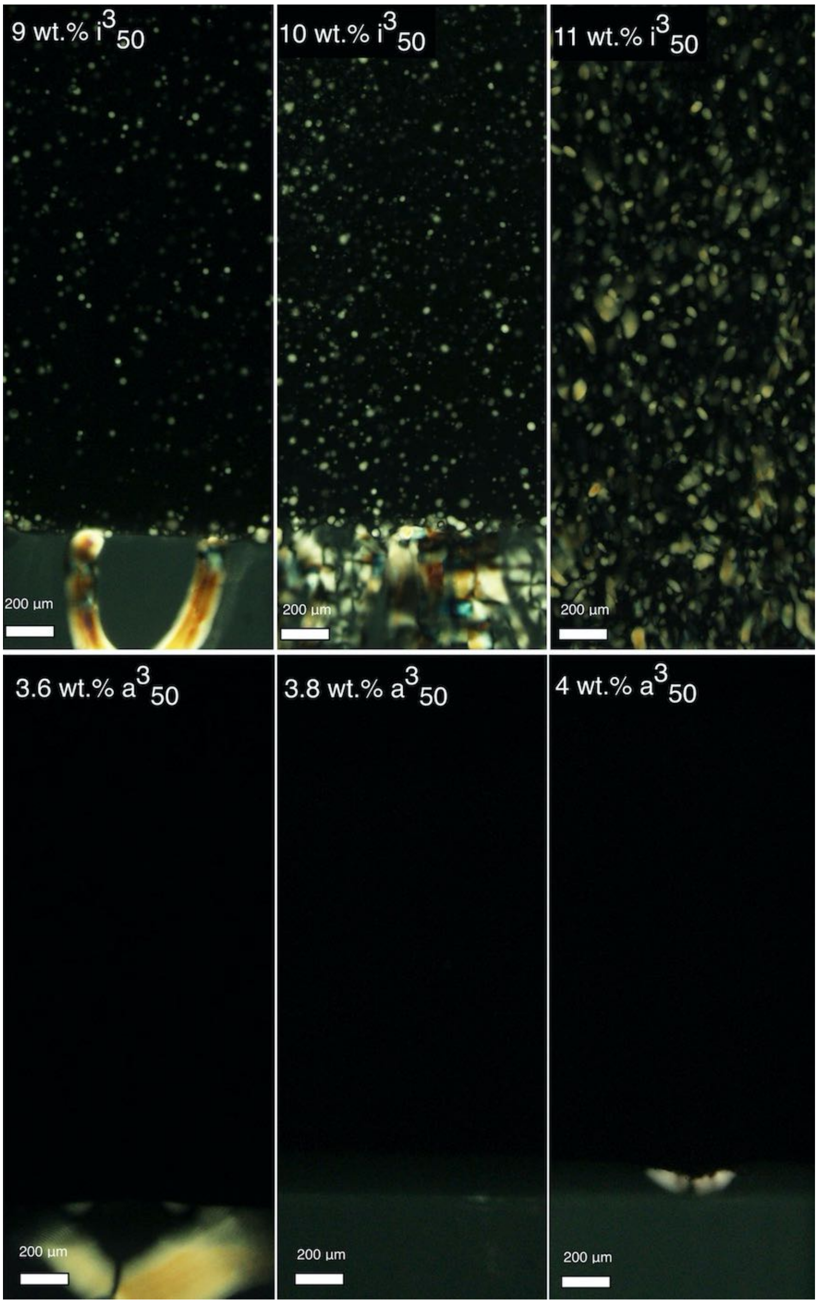

Supplementary Figure 9: Polarising optical microscopy images of vertically stored (18 months) glass capillaries filled with $i^3_{50}$ (top) and $a^3_{50}$ (bottom) fractions from the 50/50 scheme. The CNC content is chosen to roughly cover the half of the biphasic regime closer to the cholesteric boundary. The scale bars correspond to 200 $\mu$m. Gravity is downwards in all photos.

the boundary conditions and thus approach an equilibrium configuration. This is very rarely seen in unfractionated CNC suspensions.

In these flat capillaries, the large-area glass surfaces of the capillary top and bottom dominate the boundary conditions, promoting planar alignment at the glass interface, which means that the helix aligns perpendicular to the glass. Since we are observing the samples perpendicular to the capillary plane, this means that we observe the cholesteric phase along the helix. Because the helix pitch in these equilibrium samples has a pitch $p_0$ on the order of a few $\mu$m, too long to produce visible structural colour for observation along the helix, we do not see any colours from selective reflection/structural colour. However, we also do not see any effect of birefringence, because the optic axis, being defined by the director $\mathbf{n}$, rotates continuously from one sample side to the next. Instead we see optical activity, as the light polarisation is rotated by the cholesteric liquid crystal as it moves through the long-pitch helix. This gives rise to a slight increase in brightness compared to the isotropic phase, which has no effect on the polarisation. The effect is best seen in the lower row of Fig. 9.

Even in the long-rod fractions it takes long time for the helix to reach the uniform orientation perpendicular to the capillary plane throughout the full sample area. While the 18 months of waiting were enough to achieve uniform alignment in the 3.8 wt.% and 4 wt.% samples of $a^3$50 in Fig. 9, the 2 months of waiting before the photos in Fig. 8 were taken were insufficient. Regions with non-perpendicular helix orientation are easily recognized through bright defects characteristic of cholesterics, often referred to as 'oily streaks' [5], see the lower row in Fig. 8. The oily streaks are much brighter than the background because here we are not looking along the helix, hence we see strong birefringence from the cholesteric phase in these regions. In fact, the helix is typically aligned in the plane of the capillary within an oily streak, giving rise to a classical fingerprint texture [5] from which we can measure $p_0$. Examples of this procedure are provided in the following.

## Supplementary Note 6:
## Measurements of equilibrium helix pitch in capillaries

The polarising optical microscopy (POM) photos from which we established the equilibrium pitch $p_0$ as a function of CNC mass concentration, for each different fraction, are shown for the 20/80 scheme in figures 10–15. They are all taken in sample regions where the cholesteric phase developed the helix in the plane of the sample, as confirmed by a well-defined fingerprint texture [5]. The procedure for establishing $p_0$ is explained in the Methods section of the main paper.

Similar photos (not shown) were analyzed in the same way for the 50/50 series.

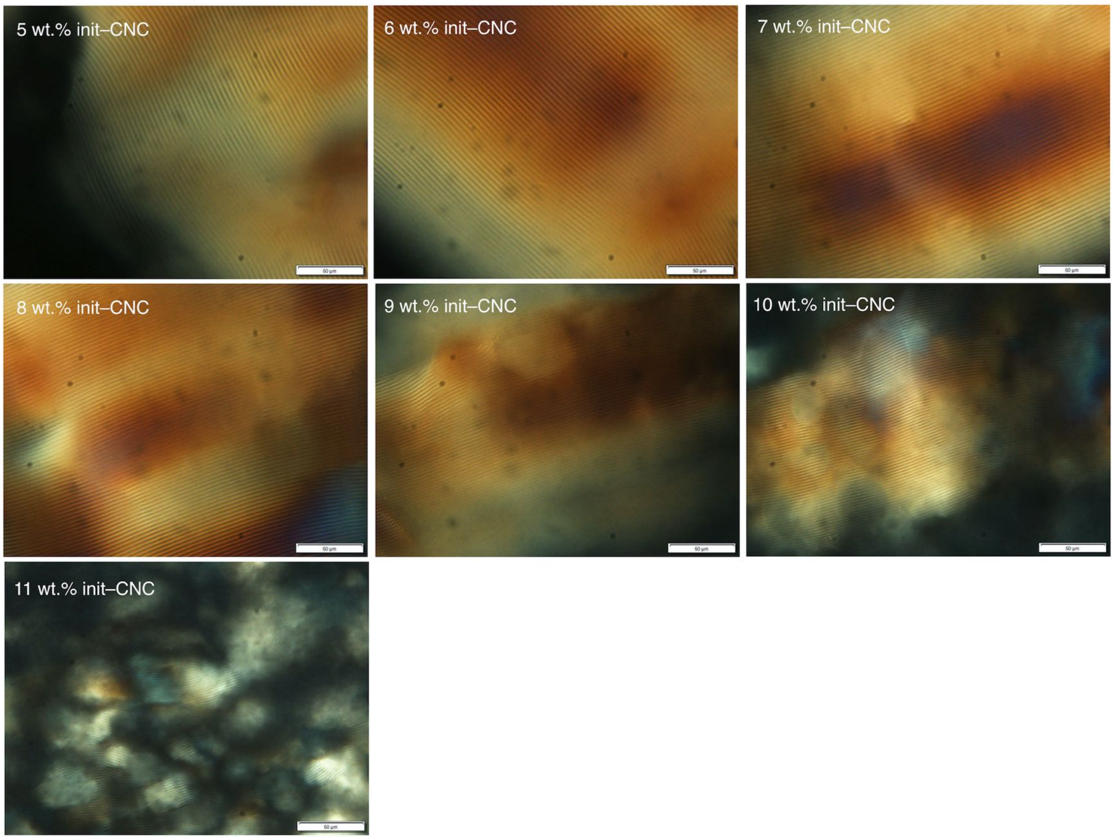

Supplementary Figure 10: POM textures for pitch measurement, with samples of $init_{20}$ in flat glass capillaries. The indicated CNC mass concentrations $W$ are for the overall sample, thus they are lower than the concentration in the cholesteric phase that is imaged whenever $W < w_1$ ($w_1 \approx 8.7$ wt.% for $init_{20}$). Scale bars correspond to 20 $\mu$m.

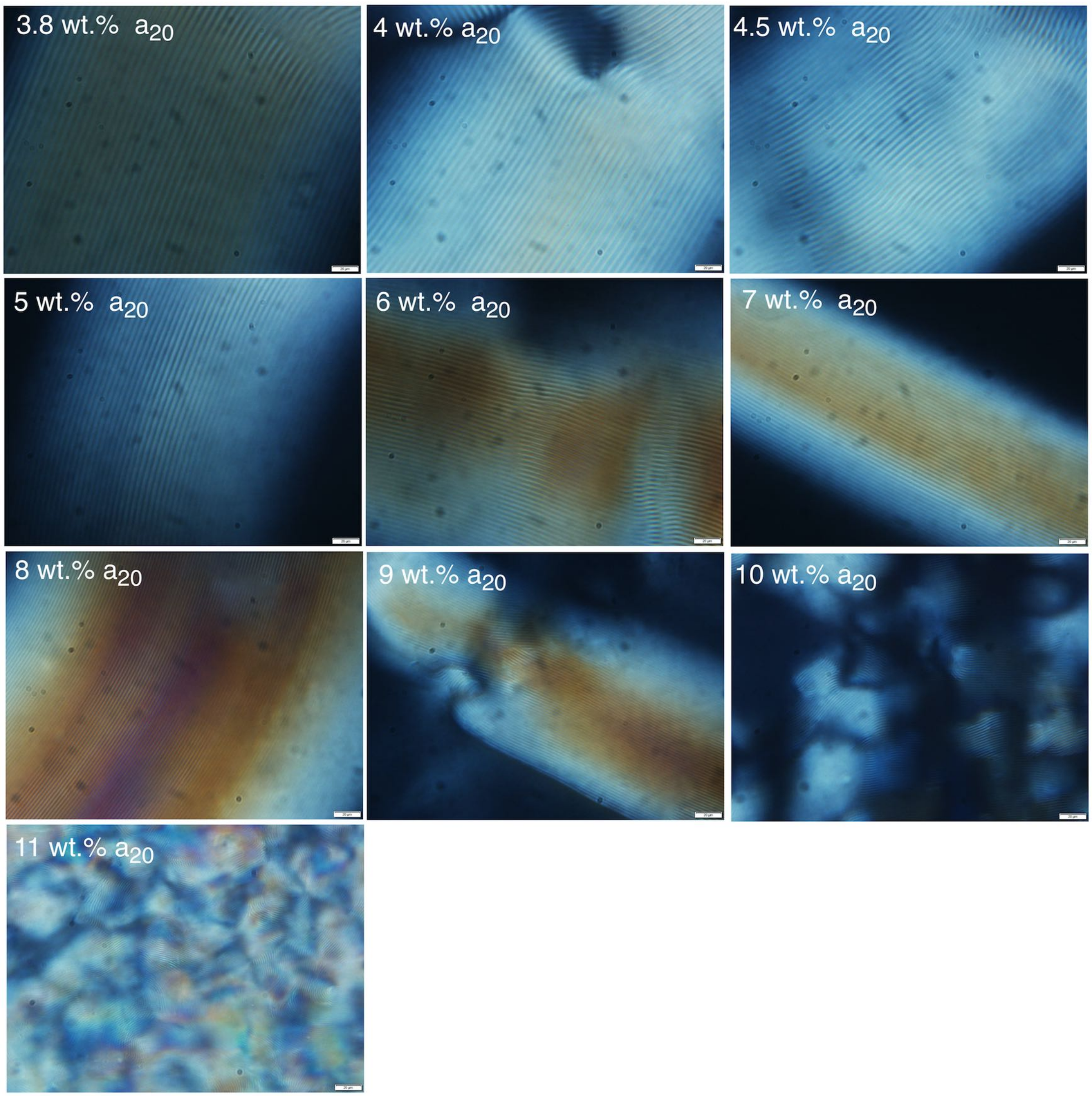

Supplementary Figure 11: POM textures for pitch measurement, with samples of $a_{20}$ in flat glass capillaries. The indicated CNC mass concentrations $W$ are for the overall sample, thus they are lower than the concentration in the cholesteric phase that is imaged whenever $W < w_1$ ($w_1 \approx 4.8$ wt.% for $a_{20}$). Scale bars correspond to 20 $\mu$m.

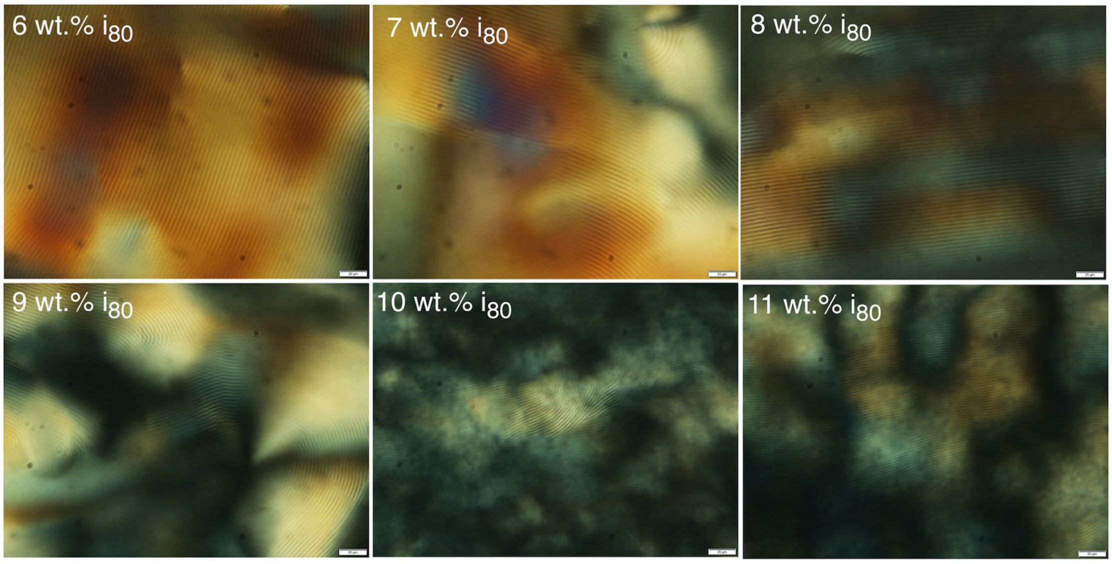

Supplementary Figure 12: POM textures for pitch measurement, with samples of $i_{80}$ in flat glass capillaries. The indicated CNC mass concentrations $W$ are for the overall sample, thus they are lower than the concentration in the cholesteric phase that is imaged whenever $W < w_1$ ($w_1 \approx 8.2$ wt.% for $i_{80}$). Scale bars correspond to 20 $\mu$m.

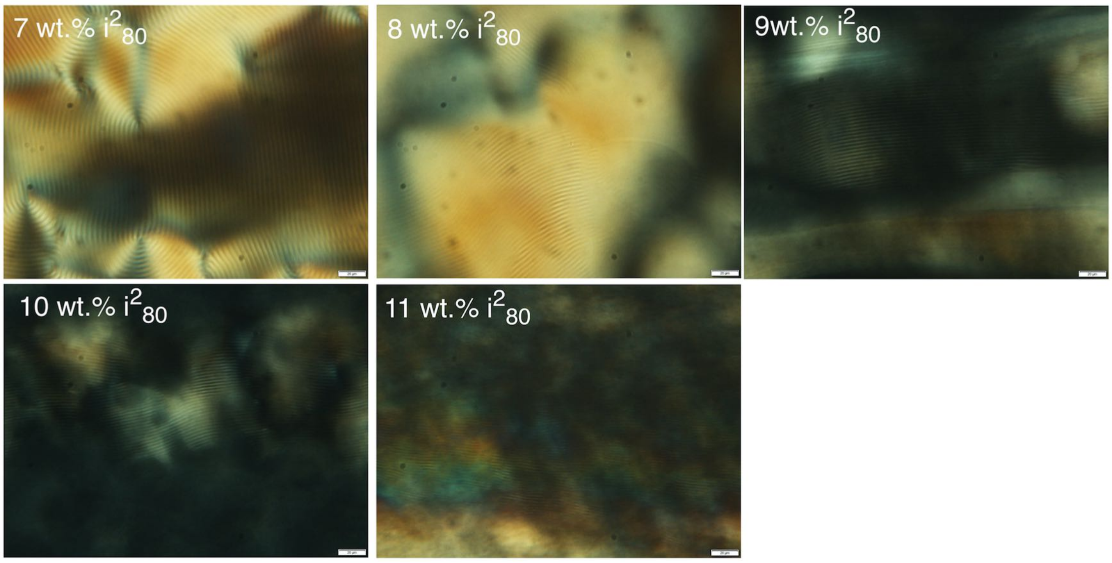

Supplementary Figure 13: Polarising optical microscopy textures for pitch measurement, with samples of $i^2_{80}$ in flat glass capillaries. The indicated CNC mass concentrations $W$ are for the overall sample, thus they are lower than the concentration in the cholesteric phase that is imaged whenever $W < w_1$ ($w_1 \approx 9.1$ wt.% for $i^2_{80}$). Scale bars correspond to 20 $\mu$m.

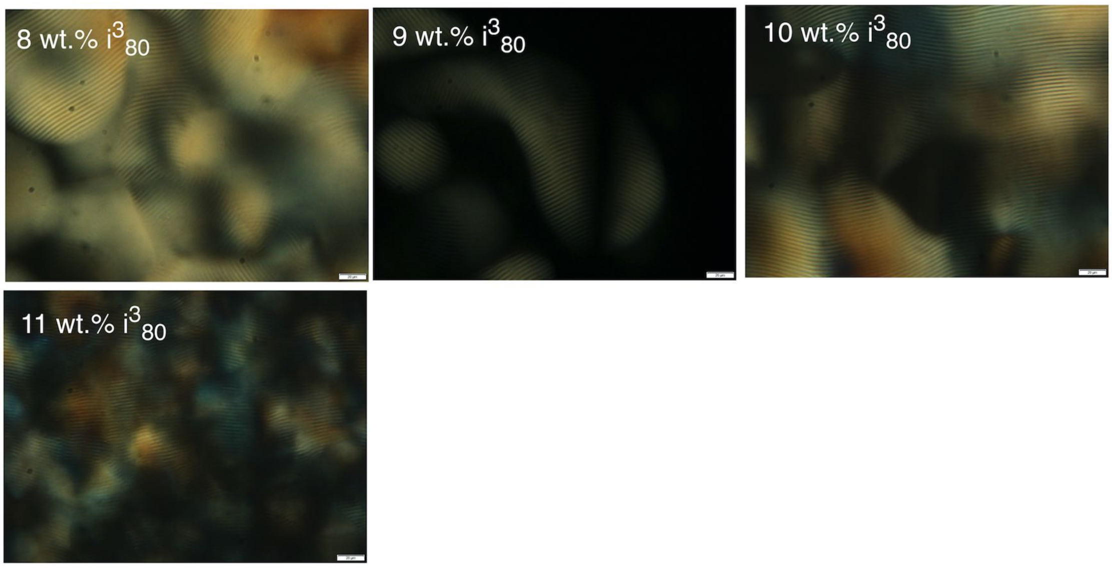

Supplementary Figure 14: POM textures for pitch measurement, with samples of $i^3_{80}$ in flat glass capillaries. The indicated CNC mass concentrations $W$ are for the overall sample, thus they are lower than the concentration in the cholesteric phase that is imaged whenever $W < w_1$ ($w_1 \approx 10$ wt.% for $i^3_{80}$). Scale bars correspond to 20 $\mu$m.

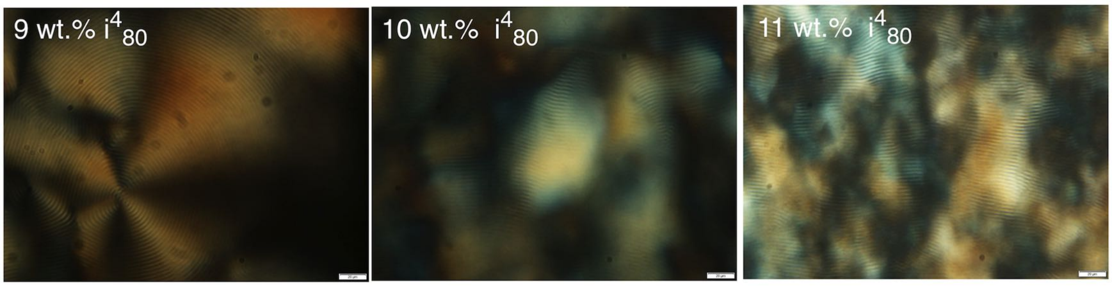

Supplementary Figure 15: POM textures for pitch measurement, with samples of $i^4_{80}$ in flat glass capillaries. The indicated CNC mass concentrations $W$ are for the overall sample, thus they are lower than the concentration in the cholesteric phase that is imaged whenever $W < w_1$ ($w_1 \approx 11$ wt.% for $i^4_{80}$). Scale bars correspond to 20 $\mu$m.

## Supplementary Note 7: Fitting of pitch versus mass concentration data for establishing Helical Twisting Power ($HTP$)

The numerical results from fitting equation (2) in the main paper to the experimental $p_0$ versus $W$ data are summarized in Table 2. The fitting results are presented graphically in Fig.4 in the main paper.

Supplementary Table 2: Tabular overview of the results from fitting Eq. (2) in the main paper to the experimental data from the six fractions for which we studied $p_0(W)$. We also reproduce the average length $\bar{L}$ as obtained from AFM, found in Table 1 in the main paper. An estimate of the standard deviation in $\bar{L}$ is given by $\varsigma\bar{L}$, where $\varsigma$ is the length dispersity as obtained by fitting the log-normal distribution to the experimental length data. For $HTP$ and $w'$ we get the respective standard deviations ($\sigma$) directly from the pitch fitting procedure.

| Fraction | $\bar{L}$, $\mu$m | $\varsigma\bar{L}$, $\mu$m | $HTP$, $\mu\text{m}^{-1}\%^{-1}$ | $\sigma(HTP)$, $\mu\text{m}^{-1}\%^{-1}$ | $w'$, wt.% | $\sigma(w')$, wt.% |
|---|---|---|---|---|---|---|
| $a_{20}$ | 0.274 | 0.047 | 0.029 | 0.003 | 1.4 | 0.5 |
| $i_{80}$ | 0.184 | 0.037 | 0.027 | 0.0081 | 2 | 2 |
| $i_{80}^2$ | 0.203 | 0.055 | 0.02 | 0.010 | 2 | 3 |
| $a_{50}^3$ | 0.270 | 0.068 | 0.042 | 0.006 | 1.8 | 0.6 |
| $a_{50}^4$ | 0.280 | 0.078 | 0.037 | 0.006 | 1.2 | 0.7 |
| $a_{50}^5$ | 0.287 | 0.062 | 0.037 | 0.004 | 1.3 | 0.5 |

## Supplementary Note 8: Comments on the linear relationship between Helical Twisting Power and CNC length

The data in Fig. 4c in the main paper shows considerable scattering and three data points show significant deviations from the linear fit. For two of these, both obtained from long-rod fractions, normally more reliable, we can find potential explanations to the discrepancies. The $HTP$ value for $a_{50}^3$ is significantly higher than predicted by Eq. (3) in the main paper, while the $a_{20}$-value is lower. Looking at the $a_{50}^3$ pitch data in Fig. 4a-b in the main paper, we see that the errors in establishing $p_0$ in this fraction are higher than for other fractions, and the experimental data points show more scattering than usual. It appears that three generations of 50/50 fractionation are not enough to bring down the rod length dispersity to levels that allow a treatment of the suspension as were it non-disperse, as we apply here.

Regarding the $a_{20}$ fraction, we attribute the discrepancy mainly to the fact that this is the very first fraction in the 20/80 scheme, obtained by letting the pristine CNC suspension sediment. Because we minimize sonication to avoid damage to the CNCs, the pristine suspension contains aggregates that are so large that they sediment individually. In other words, these aggregates, which can have shapes very different from rods and contain CNCs of very mixed character, end up in the $a_{20}$ suspension solely due to their large size and weight. They do not take part in the liquid crystal formation (they may even disturb it) but they add to the CNC mass, hence they give a systematic offset to $W$ that shifts the $a_{20}$ curves to the right in Fig. 4a-b in the main paper, resulting in an artificially low $HTP$ value. We are currently in the process of repeating the fractionation after having removed the very first sediment that is not related to liquid crystal formation; the results will be reported separately.

A key question is why $HTP$ would increase with increasing rod length, potentially following a linear relationship. Providing a definitive answer is beyond the scope of this study, but we may start the discussion with the following considerations. If we, in a cholesteric colloidal suspension, have a certain mass of cellulose distributed across four rods of average lateral dimension $d$ and length $L$, the situation in terms of chiral interactions between the rods is not the same as if the same mass of cellulose is distributed over only two rods of the same $d$ but length $2L$. First, the imperfect orientational order of (chiral) nematics means that the four rods in the first case are likely to all point in slightly different directions, and we can thus expect less strong correlation in chiral interactions between the rods than in the second case, where the rigidity of a rod at least ensures identical orientation across a length of $2L$. We saw a similar case of decreased chiral interactions for a thermotropic liquid crystal in which the molecules undergo a conformational change between straight and bent, with a much tighter helix pitch, suggesting stronger chiral interactions, when the molecules are straight [6]. Second, the (chiral) nematic phase has no positional order, hence the case with many short rods might be less effective in transmitting chiral interactions due to partial overlap between rods.

## Supplementary Note 9: Effects of varying ionic strength on the liquid crystal phase behavior of CNC suspensions

The relationship between macroscopic phase properties of liquid crystalline CNC suspensions and the mass concentration of CNC is significantly complicated by the fact that the CNCs are electrostatically stabilized, with covalently bound surface charges (negative sulphate half ester groups in our case) as well as counter ions ($Na^+$ in our case) which enter solution. This means that the concentration of free ions in solution, often described through the concept of ionic strength, changes as the mass concentration of CNC changes. This has strong impact because the effective CNC volume is not simply the volume of cellulose, but also the excluded volume afforded by the electrostatic repulsion must be added. This is quantified by the Debye screening length:

$$\kappa^{-1} = \sqrt{\frac{\epsilon_0 \epsilon_r k_B T}{q^2 N_A n}} \tag{4}$$

where $\epsilon_0$ and $\epsilon_r$ are the dielectric permittivities of vacuum and the solvent, respectively, $k_B$ is the Boltzmann constant, $T$ is the absolute temperature, $q$ is the elementary charge,

$N_A$ is Avogadro's constant, and $n$ is the concentration of free counter ions[1] in the sample, measured in mol/m$^3$, which numerically is identical to the concentration in mM.

For us, the important parameter controlling the Debye screening length is the counter ion concentration $n$, as this varies significantly in experiments, while all other parameters can be considered constant or approximately constant. We can write:

$$n = n_{CNC} + n_0 + n_{add} \tag{5}$$

where we define $n_{CNC}$ as the counter ions released by the CNC, $n_0$ as the small but non-zero concentration of counter ions in the deionized water, preventing $\kappa^{-1}$ from diverging as the CNC content goes to zero, and $n_{add}$ the concentration of counter ions that may be introduced by controlled addition of an inorganic salt, typically NaCl.

The Debye screening length is on the order of 1 nm [7], hence its effect is negligible for the CNC length but it has a strong impact on the effective lateral dimension, since this is on the same scale as $\kappa^{-1}$. In order to make calculations feasible, we will in the following describe the effective lateral dimension using a radius of an approximate cylindrical representation of a CNC, $r = d/2$. While the effective length $L^{\text{eff}}$ can thus safely be approximated by the length of the actual CNC, $L^{\text{eff}} \approx L$, the effective radius can be written $r^{\text{eff}} = r + \kappa^{-1}$. The resulting impact of $\kappa^{-1}$ on the liquid crystal behavior of the CNC suspension is twofold. On the one hand, it influences the effective aspect ratio, $L^{\text{eff}}/(2r^{\text{eff}}) \approx L/(2r+2\kappa^{-1})$. This means that the critical rod volume fractions for liquid crystal formation in the Onsager model, $\phi_0 = 3.3(2r^{\text{eff}})/L^{\text{eff}}$ and $\phi_1 = 4.5(2r^{\text{eff}})/L^{\text{eff}}$, decrease if $\kappa^{-1}$ is reduced. On the other hand, $\kappa^{-1}$ affects the relation between *effective* volume fraction $\phi$ of CNCs and their (local) mass fraction $w$, since the effective volume of one CNC in suspension can be approximated $\pi(r + \kappa^{-1})^2 L$. A decrease in $\kappa^{-1}$ thus reduces the effective volume fraction, which in terms of the critical mass fractions $w_0$ and $w_1$ would lead to an increase, thus the opposite impact. Because the volume scales as radius squared whereas the aspect ratio scales linearly with radius, one may argue that the former effect dominates [8].

It is important to realize, however, that it is not the entire effective CNC radius that is influenced by $n$, only the fraction that corresponds to $\kappa^{-1}$. To get a clearer view of the actual impact, let us formulate functions for the variation with the local[2] CNC mass concentration $w$ of the effective rod volume fraction $\phi$ as well as of the stability limit $\phi_1$ of the liquid crystal phase. The latter is critical to our analysis as it determines what the CNC content is in the liquid crystal phase once it forms. With $N$ cylindrical rods in the system, their total effective volume can be written:

$$V_{\text{CNC}}^{\text{eff}} = N\pi(r + \kappa^{-1})^2 L = \frac{w/100 \cdot m}{m_{\text{rod}}}\pi(r + \kappa^{-1})^2 L \tag{6}$$

---

[1] The relation is correct when CNCs are the only ion source, as all free ions in solution are counter ions. When adding additional salt like NaCl, as we will do in this discussion, the question of how to consider the added Cl$^-$ ions is non-trivial. For simplicity, we consider only Na$^+$ counter ions in this discussion, but the reader is advised that this is an approximation.

[2] In case the global CNC mass concentration $W$ is in the biphasic regime, the local $w$ must be defined for either the isotropic or the cholesteric phase. It must refer to a homogeneous phase.

where we introduced $m$ for the mass of a uniform CNC suspension with CNC mass concentration $w$ throughout[3] and $m_{\text{rod}}$ for the mass of a single dry approximate CNC 'rod' (acknowledging that an actual CNC has a much more complex shape than a cylindrical rod). Introducing the density of cellulose $\rho_c$, and an effective density $\rho = \rho(w)$ and the volume $V$, respectively, of the uniform CNC suspension, we can reformulate this as:

$$V_{\text{CNC}}^{\text{eff}} = \frac{w/100 \cdot \rho V}{\rho_c \pi r^2 L} \pi (r + \kappa^{-1})^2 L = \frac{w/100 \cdot \rho V}{\rho_c r^2} (r + \kappa^{-1})^2 \tag{7}$$

This gives us the effective volume fraction $\phi$ of CNC:

$$\phi = V_{\text{CNC}}^{\text{eff}} / V = \frac{w/100 \cdot \rho}{\rho_c r^2} (r + \kappa^{-1})^2 \tag{8}$$

Let us now, for simplicity, approximate the function $\rho(w)$ with a simple weighted averaging:

$$\rho(w) = w/100 \cdot \rho_c + (1 - w/100)\rho_{\text{aq}} = w/100 \cdot 1500 + (1 - w/100) \cdot 1000 = \tag{9}$$
$$= 1000 \left[ \frac{w}{100}(1.5 - 1) + 1 \right] = (1000 + 5w) \text{ kg/m}^3$$

where we have used the densities of cellulose, $\rho_c = 1500$ kg/m$^3$, and of water, $\rho_{\text{aq}} = 1000$ kg/m$^3$. This gives us, for the effective rod volume fraction:

$$\phi = \frac{w/100 \cdot (1000 + 5w)}{1500 r^2} (r + \kappa^{-1})^2 \tag{10}$$

Writing $x = w/100$, we can simplify this a bit:

$$\phi = \frac{x \cdot (1000 + 5 \cdot 100x)}{1500 r^2} (r + \kappa^{-1})^2 = \frac{500x^2 + 1000x}{1500 r^2} (r + \kappa^{-1})^2 = \frac{\frac{x^2}{2} + x}{1.5 r^2} (r + \kappa^{-1})^2 \tag{11}$$

If we now insert our expression for the Debye length, and in it our expression with the three different counter ion contributions, we obtain:

$$\phi = \frac{\frac{x^2}{2} + x}{1.5 r^2} \left( r + \sqrt{\frac{\epsilon_0 \epsilon_r k_B T}{q^2 N_A (n_{CNC} + n_0 + n_{add})}} \right)^2 \tag{12}$$

To simplify the expression we introduce $\alpha = \sqrt{\frac{\epsilon_0 \epsilon_r k_B T}{q^2 N_A}}$, yielding:

$$\phi = \frac{\frac{x^2}{2} + x}{1.5 r^2} \left( r + \frac{\alpha}{\sqrt{n_{CNC} + n_0 + n_{add}}} \right)^2 \tag{13}$$

Next, we assume that every unit mass CNC releases the same amount of counter ions into solution, regardless of $x$, which means that we can write $n_{CNC} = Cx$, where $C$

---

[3] In case the global CNC mass concentration $W$ is in the biphasic regime, the fraction with mass $m$ could be chosen either as the isotropic or the cholesteric fraction, but it cannot contain both.

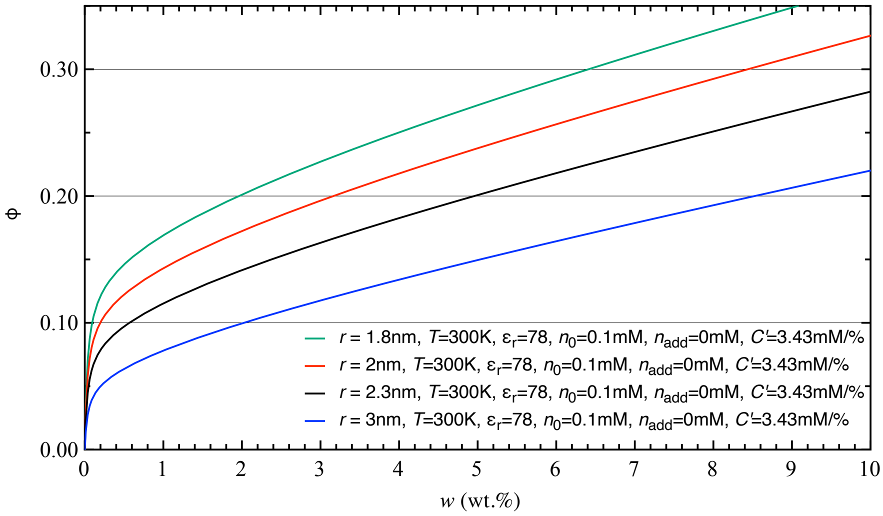

Supplementary Figure 16: Effective volume fraction of suspended (hydrated) CNCs as a function of CNC mass concentration $w$ in a uniform CNC suspension. The larger the apparent CNC rod radius, the lower the effective volume fraction at the same CNC mass fraction, a result of the fact that a certain mass of 'thin' CNCs has more total excluded volume from electrostatic repulsion than the same mass of 'thick' CNCs, which have less surface to the water.

is a constant. Conductometric titration showed that the sulphur content is 1.1 wt.% of the CNC mass for the batch used for the salt addition experiments (see [1] for the batch characterization), and since we have one Na$^+$ counter ion for every sulphur atom on the CNC surface (the surface charges are due to sulphate half ester groups) we can equate the number of moles of sulphur with the number of moles of Na$^+$ ions. Approximating the density $\rho$ of the CNC suspension as 1 kg/L, denoting the mass and volume of the CNC suspension as $m$ and $V$, respectively, this allows us to estimate $n_{CNC}$ and $C$:

$$n_{CNC} = [Na^+] = [S] = \frac{n_S}{V} = \frac{m_S/M_S}{m/\rho} = \frac{0.011 m_{CNC}/M_S}{m} = \frac{0.011 wm/100/M_S}{m} = \\ = \frac{1.1 \cdot 10^{-4}}{32.065 \cdot 10^{-6}\ \text{kg/mmol}} w = 3.43 w\ \text{mM} = 343 x\ \text{mM} \tag{14}$$

If we at this point assume that no inorganic salt is added, thus $n_{add} = 0$, we get:

$$\phi^{\text{no salt}} = \frac{\frac{x^2}{2} + x}{1.5 r^2} \left( r + \frac{\alpha}{\sqrt{Cx + n_0}} \right)^2 \tag{15}$$

We plot this function, using $C = 343$ mM, as a function of $w = 100x$ in Fig. 16.

For the variation with $n$ of the critical volume fraction $\phi_1$, we first write $\phi_1$ using Onsager's criterion applied to a 'rod' aspect ratio that includes the radius addition by the Debye screening length:

$$\phi_1(x_1) = 4.5 \cdot 2r^{\text{eff}}/L = \frac{9}{L}(r + \kappa^{-1}(x_1)) = \frac{9}{L}\left(r + \frac{\alpha}{\sqrt{Cx_1 + n_0}}\right) \tag{16}$$

where we have introduced $x_1 = w_1/100$ as the CNC mass fraction in the liquid crystal phase as it starts forming. Since equation (15) gives a general relation between $\phi$ and $x$, we can set $x = x_1$ in (15) and equalize it to (16):

$$\phi_1 = \frac{\frac{x_1^2}{2} + x_1}{1.5r^2}\left(r + \frac{\alpha}{\sqrt{Cx_1 + n_0}}\right)^2 = \frac{9}{L}\left(r + \frac{\alpha}{\sqrt{Cx_1 + n_0}}\right) \tag{17}$$

$$\Leftrightarrow L\frac{\frac{x_1^2}{2} + x_1}{13.5r^2}\left(r + \frac{\alpha}{\sqrt{Cx_1 + n_0}}\right) = 1$$

In Fig. 17, we plot the left-hand side (LHS) as a function of $w$ for four different apparent CNC radii and, for $r = 2.3$ nm, for three different CNC lengths. The $r = 2.3$ nm plots are very close to our experimental findings. Wherever the left-hand side curve crosses the grid-line representing $LHS = 1$, we have our expected $w_1$ value.

Let us now move to the case where NaCl salt is added (considering only the effect of the Na$^+$ ions). We can, first, extend equation (15) to also include the effect of NaCl addition:

$$\phi^{\text{with salt}} = \frac{\frac{x^2}{2} + x}{1.5r^2}\left(r + \frac{\alpha}{\sqrt{Cx + n_0 + n_{add}}}\right)^2 \tag{18}$$

and the corresponding extension of equation (17) yields:

$$L\frac{\frac{x_1^2}{2} + x_1}{13.5r^2}\left(r + \frac{\alpha}{\sqrt{Cx_1 + n_0 + n_{add}}}\right) = 1 \tag{19}$$

Setting $L = 300$ nm and $r = 2.3$ nm, corresponding quite well to our experiments with added NaCl, we plot in Fig. 18 the left-hand side of (19) for no added salt and for the three added salt concentrations of the experiment described in Fig. 5a of the main paper. We here zoom in on the $w$-range of interest, showing that the stability limit of the chiral nematic phase increases from $w_1 \approx 3.9$ wt.% to approximately 4.2, 4.4 and 4.7 wt.%, respectively, for the three concentrations of added NaCl.

But perhaps more interesting is to consider the special case where we ensure that the total counter ion concentration has a constant value $n_{fix}$ by adding NaCl. At the same time we assume that the counter ion concentration of the pure water is negligible in comparison, i.e $n_0 \ll n_{fix}$, hence we consider $n_{fix} \approx Cx + n_{add}$. Because $n_{add}$ is always positive, we can only do this study for values of $x$ that are lower than that which gives $Cx = n_{fix}$, but for all these values, we can now write the volume fraction and the critical volume fraction simply as:

$$\phi^{n=n_{fix}} = \frac{\frac{x^2}{2} + x}{1.5r^2}\left(r + \frac{\alpha}{\sqrt{n_{fix}}}\right)^2 = \frac{x^2 + 2x}{3}\frac{K^2}{r^2} \tag{20}$$

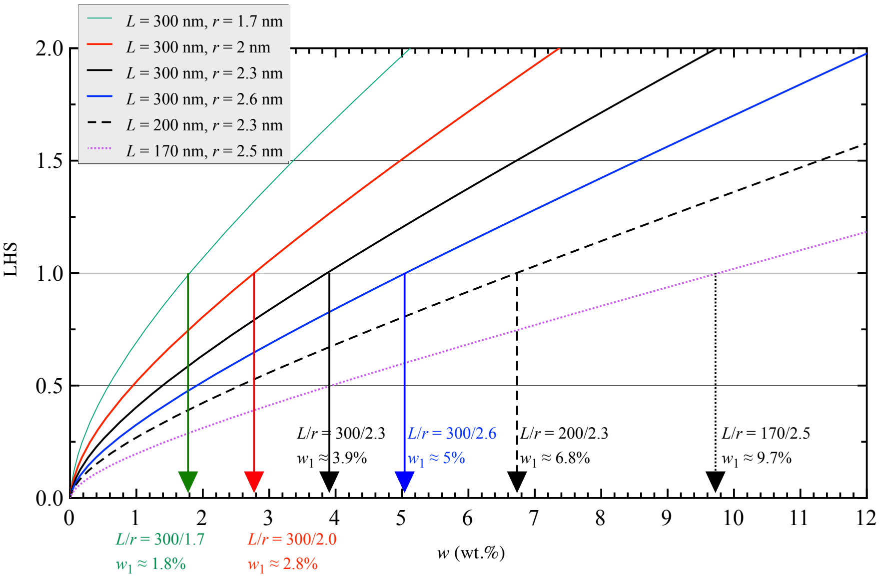

Supplementary Figure 17: Graphical solution of the $\phi_1(w)$ relationship, equation (17), with no added salt, for different CNC lengths and apparent radii. The results match our direct experimental findings for $L \approx 300$ nm and $r \approx 2.3$ nm very well. For $L \approx 170$ nm and $r = 2.5$ nm, we reproduce the $w_1$ value estimated for short CNCs based on the electron microscopy analysis of the dried film, as discussed in the main paper. The predicted $w_1$ value for short rods is much higher than that obtained from the phase separation experiments, most likely due to the high viscosity and slow phase separation in suspensions of short CNCs making this method unreliable for short-rod suspensions.

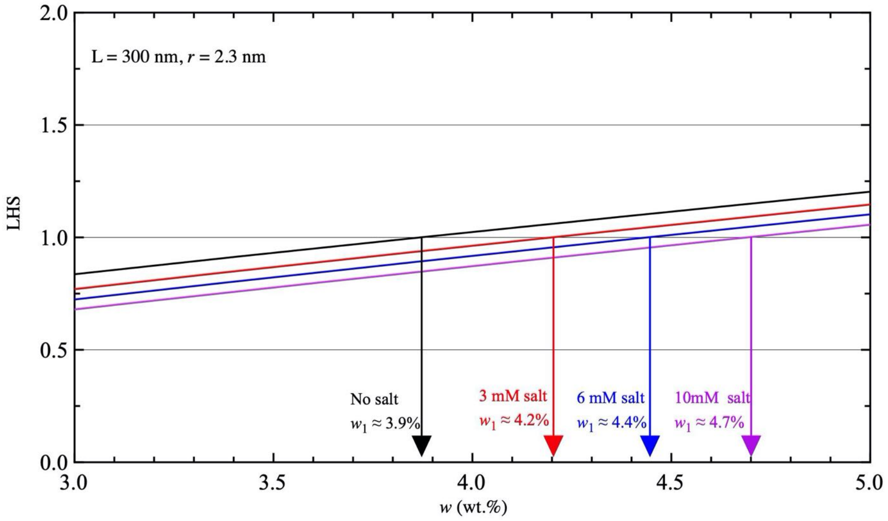

Supplementary Figure 18: Graphical solution of the $\phi_1(w)$ relationship, equation (19), for CNC parameters representative of our experiments, with no added salt as well as with the three different added salt concentrations used in the experiment of Fig. 5a in the main paper.

and

$$\phi_1^{n=n_{fix}} = \frac{9}{L}\left(r + \frac{\alpha}{\sqrt{n_{fix}}}\right) = \frac{9K}{L} \tag{21}$$

where we introduced the rescaled constant $K = r + \frac{\alpha}{\sqrt{n_{fix}}}$. Note that $\phi_1^{n=n_{fix}}$ no longer depends on $x_1$, since the constant counter ion condition ensures that the effective rod geometry and volume are constant. Instead, it depends critically on $n_{fix}$. Thus, to find the CNC mass concentration at which the liquid crystal phase forms when we have fixed the total counter ion concentration to $n_{fix}$, we write:

$$\phi_1^{n=n_{fix}} = \frac{x_1^2 + 2x_1}{3}\frac{K^2}{r^2} = \frac{9K}{L} \tag{22}$$

$$\Leftrightarrow x_1^2 + 2x_1 = \frac{27r^2}{KL}$$

$$\Leftrightarrow x_1^2 + 2x_1 - \frac{27r^2}{KL} = 0$$

We solve this second-order equation to get:

$$x_1 = -1 \pm \sqrt{1 + \frac{27r^2}{KL}} \tag{23}$$

Since $x \geq 0$ we can reject the negative solution. Re-inserting the expression for $K$ we get:

$$x_1 = -1 + \sqrt{1 + \frac{27r^2}{(r + \frac{\alpha}{\sqrt{n_{fix}}})L}} \tag{24}$$

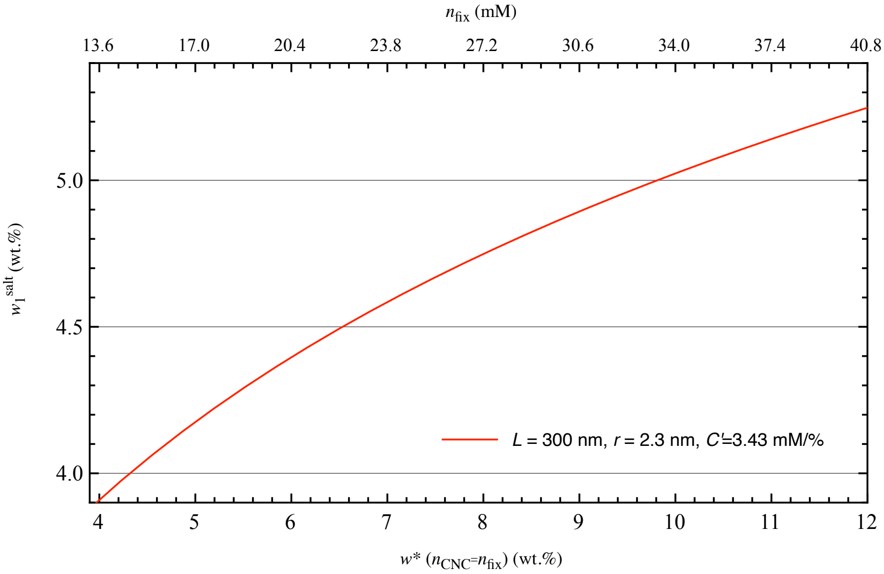

Supplementary Figure 19: The calculated variation of $w_1$ with salt added to the system to achieve a constant counter ion concentration $n_{fix}$ (displayed along the top $x$-axis), as a function of the CNC mass fraction concentration $w^*$ giving $n_{CNC} = n_{fix}$.

What interests us particularly is how salt addition to different constant $n_{fix}$ values change $w_1$ compared to when no salt is added. Since the maximum CNC mass concentration $w^*$ during constant counter ion concentration suspensions is that which gives a counter ion concentration $n_{fix}$ without any added salt, i.e. $n_{CNC}@w^* = n_{fix}$, we plot $w_1^{salt}$ as a function of $n_{fix}$, or of $w^*$, in Fig. 19. We see that, while $w_1$ decreases by the salt addition, the effect is not too dramatic. Specifically, for the three values of $n_{fix}$ for which we did experimental tests, $n_{fix}^1 = 31$, $n_{fix}^2 = 34$ and $n_{fix}^3 = 38$ mM, respectively, we get $w_1$ values of 4.9, 5.0 and 5.1 wt.%, respectively.

## Supplementary Note 10:
## Estimation of the cellulose volume fraction at kinetic arrest

The compression of the helix during evaporation of the remaining water after kinetic arrest is calculated, following Frka-Petesic et al. [9], under the assumption that no horizontal shrinkage takes place, i.e. the sessile droplet is pinned to the substrate, allowing shrinkage only in the vertical direction. Considering the extreme case of maximum helix compression, we assume that the helix is vertical, oriented along the compression axis, and that in the final dry film the CNCs are stacked directly on top of each other, without any voids. This means that the height of the final film is proportional to the volume of cellulose in the system at kinetic arrest, $V_{CNC}^k$, whereas the height at kinetic arrest is proportional, by the same factor, to the volume of cellulose plus the volume of water at kinetic arrest, $V_{aq}^k$. To establish the compression, we thus need to establish the volume fraction $\phi_k'$ of the pure CNCs (the prime signifies that there is no addition due to Debye screening; the regular rod volume fraction $\phi$ includes this additional volume) at kinetic arrest, using the knowledge that $w_k \approx 12$ wt.%:

$$\phi_k' = \frac{V_{CNC}^k}{V_{CNC}^k + V_{aq}^k} = \frac{w_k/\rho_{CNC}}{w_k/\rho_{CNC} + (100 - w_k)/\rho_{aq}} = \frac{12/1.5}{12/1.5 + 88} = 8/96 \approx 0.083 \quad (25)$$

Here we have also introduced the densities of cellulose, $\rho_{CNC}$ and of water, $\rho_{aq}$, respectively. From this consideration we obtain a vertical compression $1/\phi_k' \approx 12$ %.

## Supplementary Note 11:
## Optical microscopy images of dried CNC films

CNC films were prepared by drying droplets of $i_{50}^4$ (short CNCs) and $a_{50}^5$ (long CNCs) suspensions at $W = 3$ wt.% and 6 wt.% CNC mass concentration, respectively. After depositing a droplet (2 $\mu$L) of each starting suspension on the glass substrate, it was covered by a thin layer of hexadecane oil to prevent direct evaporation of water, instead having slow water diffusion into the oil phase before evaporating. The films were investigated by polarising optical microscopy (POM), giving the photos shown in Fig. 20 ($W = 3$ wt.% ) and Fig. 21 ($W = 6$ wt.%). Zoomed-in excerpts of these images are shown and discussed in the main paper.

## Supplementary Note 12:
## Electron microscopy images of fractured dried CNC films

Selected dry films were fractured, as described in the main paper, and the fracture surfaces were imaged by scanning electron microscopy (SEM) to reveal the periodic structure resulting from the helically modulated director in the cholesteric phase, compressed during drying. The resulting images are shown in Fig. 22 and Fig. 23. In the zoomed-in images, we also draw lines in each place where the periodicity was measured, the number next to the line indicating how many pitches are covered by the line. The resulting average pitches and standard deviations, written below the respective images, arise from averaging the pitch values calculated from each line. For the long CNCs $n = 27$ pitch values were measured, for the short CNCs, $n = 15$ pitch values were measured.

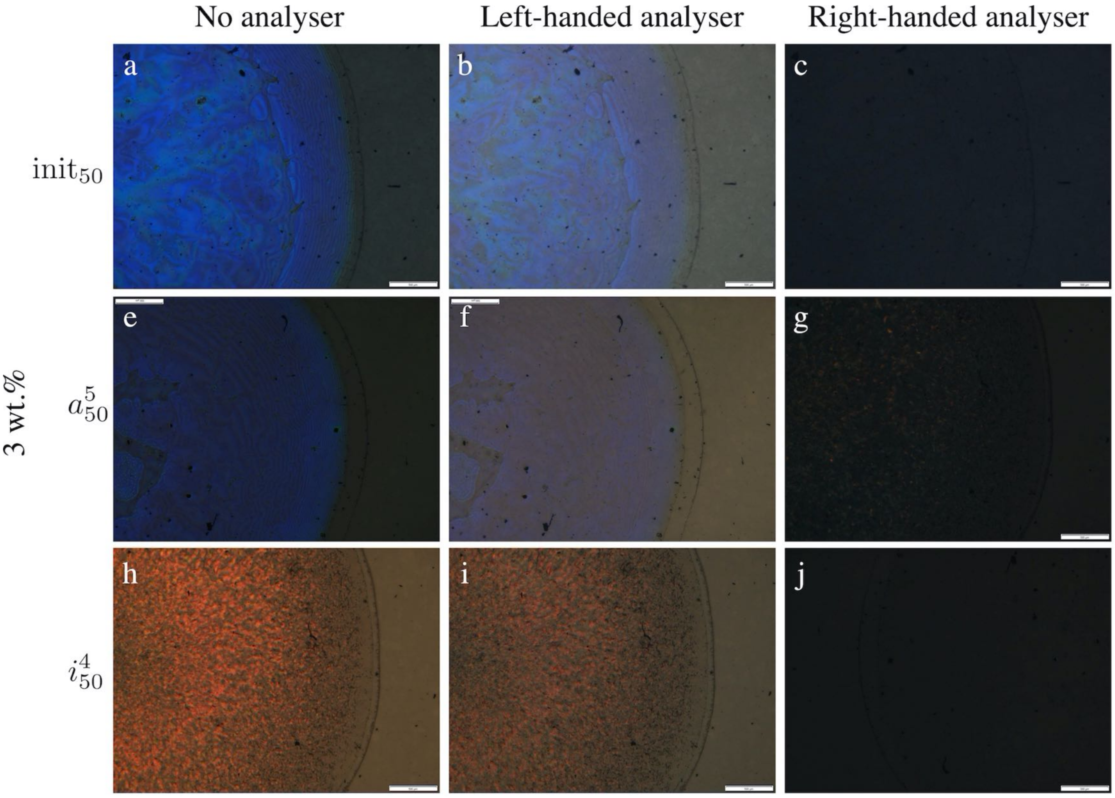

Supplementary Figure 20: Polarising optical microscopy (POM) images, obtained in reflection, of dry CNC films produced by drying low-concentration ($W = 3$ wt.%) suspensions of $i^4_{50}$ (short-CNC fraction), $a^5_{50}$ (long-CNC fraction) as well as the unfractionated CNC ($init_{50}$). All scale bars are 500 $\mu$m.

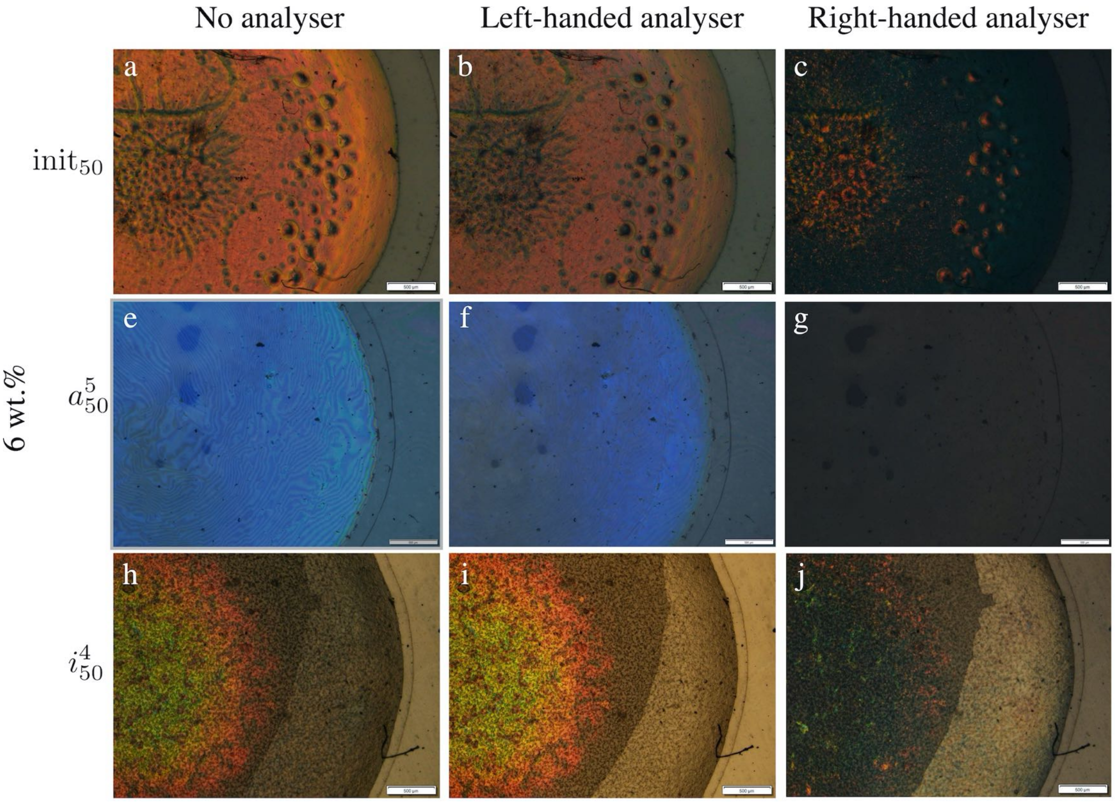

Supplementary Figure 21: Polarising optical microscopy (POM) images, obtained in reflection, of dry CNC films produced by drying medium-concentration ($W = 6$ wt.%) suspensions of $i^4_{50}$ (short-CNC fraction), $a^5_{50}$ (long-CNC fraction) as well as the unfractionated CNC ($init_{50}$). All scale bars are 500 $\mu$m.

# Film from $a_{50}^{5}$ (long CNCs)

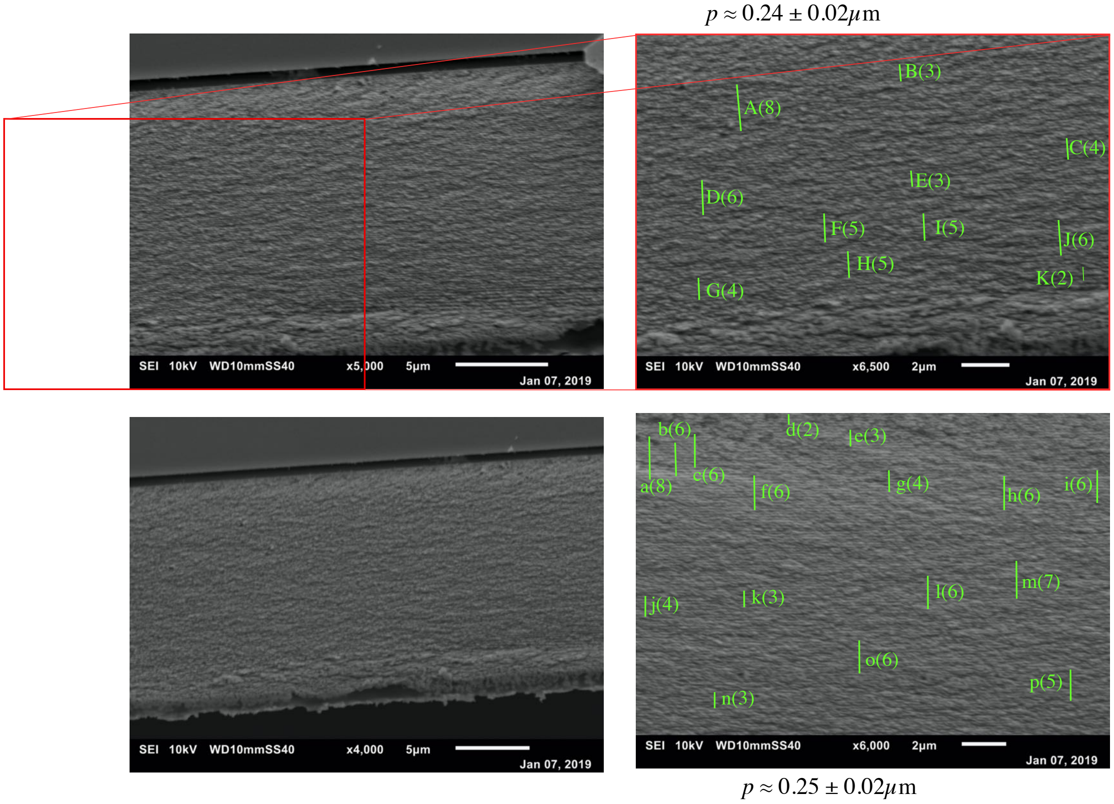

Averaging over all measurements (both images): $p \approx 0.25 \pm 0.02\mu$m

Supplementary Figure 22: SEM images of a fractured film dried from a $W = 3$ wt.% suspension of the $a_{50}^{5}$ fraction. In the most magnified images from each film we have drawn multiple lines along which the helix pitch can be measured, extending each line over as many pitches as possible (the number is written in the label).

# Film from $i_{50}^{4}$ (short CNCs)

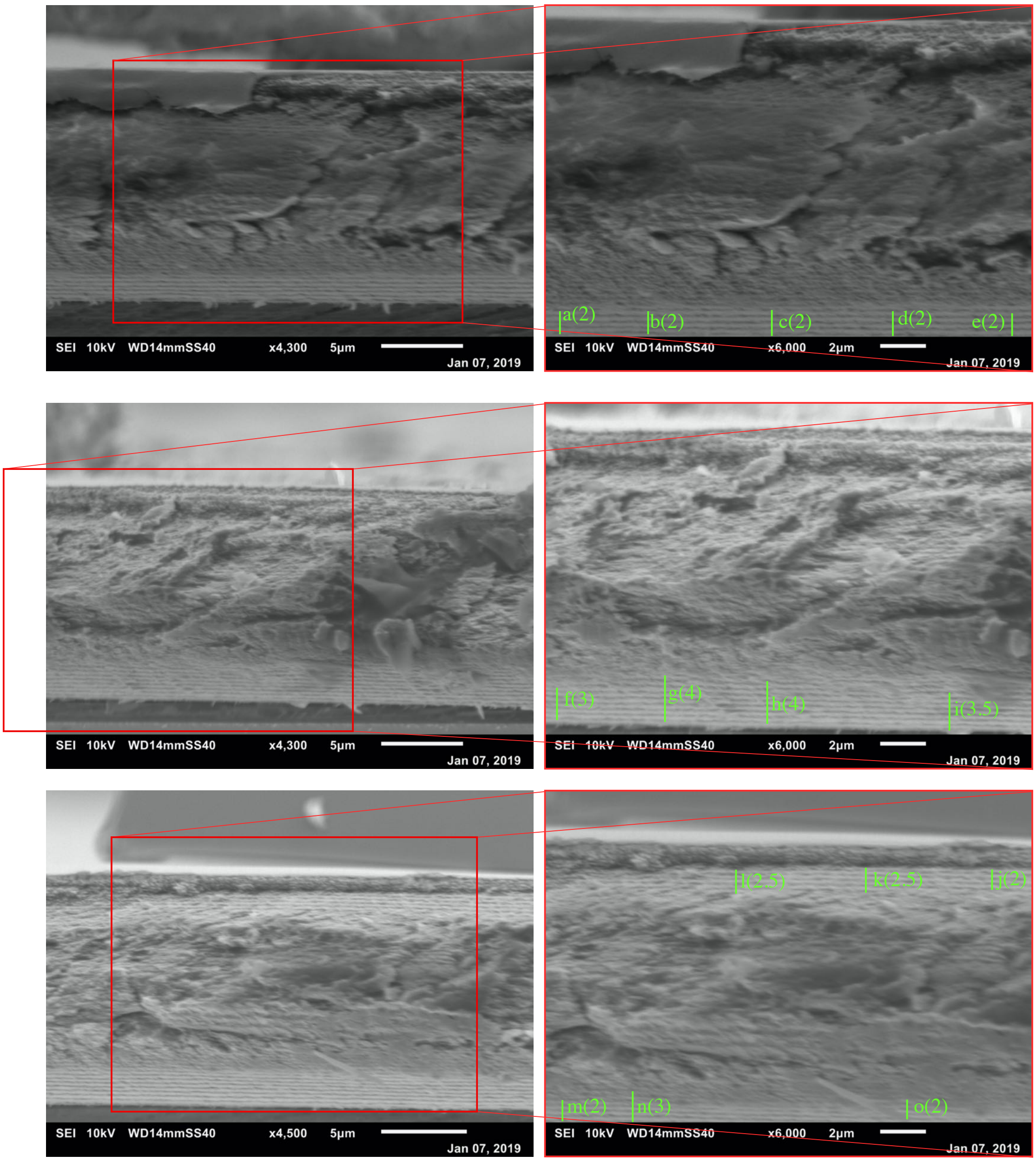

$$p \approx 0.48 \pm 0.04 \mu\text{m}$$

Supplementary Figure 23: SEM images of a fractured film dried from a $W = 3$ wt.% suspension of the $i_{50}^{4}$ fraction. In the most magnified images from each film we have drawn multiple lines along which the helix pitch can be measured, extending each line over as many pitches as possible (the number is written in the label).

# Supplementary References

[1] C. Honorato-Rios, C. Lehr, C. Schütz, R. Sanctuary, M. A. Osipov, J. Baller, and J. P. F. Lagerwall, “Fractionation of cellulose nanocrystals: enhancing liquid crystal ordering without promoting gelation,” *NPG Asia Materials*, vol. 10, pp. 455–465, 2018.

[2] S. Beck, M. Méthot, and J. Bouchard, “General procedure for determining cellulose nanocrystal sulfate half-ester content by conductometric titration,” *Cellulose*, vol. 22, no. 1, pp. 101–116, 2015.

[3] I. Usov, G. Nyström, J. Adamcik, S. Handschin, C. Schütz, A. Fall, L. Bergström, and R. Mezzenga, “Understanding nanocellulose chirality and structure-properties relationship at the single fibril level.,” *Nat. Commun.*, vol. 6, p. 7564, 2015.

[4] J. Majoinen, J. Haataja, D. Appelhans, A. Lederer, A. Olszewska, J. Seitsonen, V. Aseyev, E. Kontturi, H. Rosilo, M. Österberg, N. Houbenov, and O. Ikkala, “Supracolloidal multivalent interactions and wrapping of dendronized glycopolymers on native cellulose nanocrystals.,” *J. Am. Chem. Soc.*, vol. 136, no. 3, pp. 866–869, 2014.

[5] I. Dierking, *Textures of liquid crystals.* Weinheim: Wiley-VCH, 2003.

[6] J. P. F. Lagerwall, F. Giesselmann, M. D. Wand, and D. M. Walba, “A chameleon chiral polar liquid crystal: Rod-shaped when nematic, bent-shaped when smectic,” *Chem. Mater.*, vol. 16, no. 19, pp. 3606–3615, 2004.

[7] J. N. Israelachvili, *Intermolecular and Surface Forces, Third Edition.* Burlington, MA, USA: Academic Press, 2010.

[8] C. Honorato-Rios, A. Kuhnhold, J. R. Bruckner, R. Dannert, T. Schilling, and J. P. Lagerwall, “Equilibrium liquid crystal phase diagrams and detection of kinetic arrest in cellulose nanocrystal suspensions,” *Frontiers in Materials*, vol. 3, p. 21, 2016.

[9] B. Frka-Petesic, G. Kamita, G. Guidetti, and S. Vignolini, “Angular optical response of cellulose nanocrystal films explained by the distortion of the arrested suspension upon drying,” *Physical Review Materials*, vol. 3, no. 4, p. 045601, 2019.